Research Article | Vol. 9, No. 2 | 1 Feb 2018 | BIOMEDICAL OPTICS EXPRESS 636
Biomedical Optics EXPRESS

Novel endoscope with increased depth of field for imaging human nasal tissue by microscopic optical coherence tomography

HINNERK SCHULZ-HILDEBRANDT,[1,2,3,*] MARIO PIEPER,[2,4] CHARLOTTE STEHMAR,[1] MARTIN AHRENS,[1,2] CHRISTIAN IDEL,[5] BARBARA WOLLENBERG,[2,5] PETER KÖNIG,[2,4] AND GEREON HÜTTMANN[1,2,3]

[1]*Institute for Biomedical Optics, University of Lübeck, Peter-Monnik-Weg 4, 23562 Lübeck, Germany*
[2]*Airway Research Center North (ARCN), German Center for Lung Research (DZL), 22927 Großhansdorf, Germany*
[3]*Medical Laser Center Lübeck GmbH, Peter-Monnik-Weg 4, 23562 Lübeck, Germany*
[4]*Institute of Anatomy, University of Lübeck, Ratzeburger Allee 160, 23562 Lübeck, Germany*
[5]*ENT Clinics, University Hospital Schleswig-Holstein, Ratzeburger Allee 160, 23562 Lübeck, Germany*
[*]*hsh@bmo.uni-luebeck.de*

Abstract: Intravital microscopy (IVM) offers the opportunity to visualize static and dynamic changes of tissue on a cellular level. It is a valuable tool in research and may considerably improve clinical diagnosis. In contrast to confocal and non-linear microscopy, optical coherence tomography (OCT) with microscopic resolution (mOCT) provides intrinsically cross-sectional imaging. Changing focus position is not needed, which simplifies especially endoscopic imaging. For in-vivo imaging, here we are presenting endo-microscopic OCT (emOCT). A graded-index-lens (GRIN) based 2.75 mm outer diameter rigid endoscope is providing 1.5 – 2 µm nearly isotropic resolution over an extended field of depth. Spherical and chromatic aberrations are used to elongate the focus length. Simulation of the OCT image formation, suggests a better overall image quality in this range compared to a focused Gaussian beam. Total imaging depth at a reduced sensitivity and lateral resolution is more than 200 µm. Using a frame rate of 80 Hz cross-sectional images of concha nasalis were demonstrated in humans, which could resolve cilial motion, cellular structures of the epithelium, vessels and blood cells. Mucus transport velocity was successfully determined. The endoscope may be used for diagnosis and treatment control of different lung diseases like cystic fibrosis or primary ciliary dyskinesia, which manifest already at the nasal mucosa.

OCIS codes: (110.0110) Imaging systems; (110.4500) Optical coherence tomography; (120.3890) Medical optics instrumentation; (170.0170) Medical optics and biotechnology; (170.2150) Endoscopic imaging.

References and links

1. J. Blake, "On the movement of mucus in the lung," J. Biomech. **8**(3-4), 179–190 (1975).
2. V. Huck, C. Gorzelanny, K. Thomas, V. Getova, V. Niemeyer, K. Zens, T. R. Unnerstall, J. S. Feger, M. A. Fallah, D. Metze, S. Ständer, T. A. Luger, K. Koenig, C. Mess, and S. W. Schneider, "From morphology to biochemical state - intravital multiphoton fluorescence lifetime imaging of inflamed human skin," Sci. Rep. **6**(1), 22789 (2016).
3. M. Rajadhyaksha, A. Marghoob, A. Rossi, A. C. Halpern, and K. S. Nehal, "Reflectance confocal microscopy of skin in vivo: From bench to bedside," Lasers Surg. Med. **49**(1), 7–19 (2017).
4. E. Omar, "Current concepts and future of noninvasive procedures for diagnosing oral squamous cell carcinoma-a systematic review," Head Face Med. **11**(1), 6 (2015).
5. W. M. Petroll and D. M. Robertson, "In Vivo Confocal Microscopy of the Cornea: New Developments in Image Acquisition, Reconstruction, and Analysis Using the HRT-Rostock Corneal Module," Ocul. Surf. **13**(3), 187–203 (2015).
6. L. L. Lim, J. Xie, C. C. Chua, T. Wong, L. T. Hoang, M. D. Becker, E. B. Suhler, J. T. Rosenbaum, and F. Mackensen, "In Vivo Laser Confocal Microscopy Using the HRT-Rostock Cornea Module: Diversity and Diagnostic Implications in Patients with Uveitis," Ocul. Immunol. Inflamm. **1080**, 1–10 (2017).
7. C. MacAulay, P. Lane, and R. Richards-Kortum, "In vivo pathology: microendoscopy as a new endoscopic imaging modality," Gastrointest. Endosc. Clin. N. Am. **14**(3), 595–620 (2004).

#313807 https://doi.org/10.1364/BOE.9.000636
Journal © 2018 Received 21 Nov 2017; revised 29 Dec 2017; accepted 8 Jan 2018; published 16 Jan 2018

Biomedical Optics EXPRESS

8. T. D. Wang, S. Friedland, P. Sahbaie, R. Soetikno, P. L. Hsiung, J. T. Liu, J. M. Crawford, and C. H. Contag, "Functional imaging of colonic mucosa with a fibered confocal microscope for real-time in vivo pathology," Clin. Gastroenterol. Hepatol. **5**(11), 1300–1305 (2007).
9. F. Knieling and M. J. Waldner, "Light and sound - emerging imaging techniques for inflammatory bowel disease," World J. Gastroenterol. **22**(25), 5642–5654 (2016).
10. M. Goetz, A. Hoffman, P. R. Galle, M. F. Neurath, and R. Kiesslich, "Confocal laser endoscopy: new approach to the early diagnosis of tumors of the esophagus and stomach," Future Oncol. **2**(4), 469–476 (2006).
11. D. Huang, E. A. Swanson, C. P. Lin, J. S. Schuman, W. G. Stinson, W. Chang, M. R. Hee, T. Flotte, K. Gregory, C. A. Puliafito, and J. G. Fujimoto, "Optical Coherence Tomography," Science **254**(5035), 1178–1181 (1991).
12. A. F. Fercher, "Optical coherence tomography - development, principles, applications," Z. Med. Phys. **20**(4), 251–276 (2010).
13. J. A. Izatt, M. R. Hee, G. M. Owen, E. A. Swanson, and J. G. Fujimoto, "Optical coherence microscopy in scattering media," Opt. Lett. **19**(8), 590–592 (1994).
14. W. Drexler, U. Morgner, R. K. Ghanta, F. X. Kärtner, J. S. Schuman, and J. G. Fujimoto, "Ultrahigh-resolution ophthalmic optical coherence tomography," Nat. Med. **7**(4), 502–507 (2001).
15. R. Ansari, C. Myrtus, R. Aherrahrou, J. Erdmann, A. Schweikard, and G. Hüttmann, "Ultrahigh-resolution, high-speed spectral domain optical coherence phase microscopy," Opt. Lett. **39**(1), 45–47 (2014).
16. R. Ansari, C. Buj, M. Pieper, P. König, A. Schweikard, and G. Hüttmann, "Micro-anatomical and functional assessment of ciliated epithelium in mouse trachea using optical coherence phase microscopy," Opt. Express **23**(18), 23217–23224 (2015).
17. M. Pieper, H. Schulz-Hildebrandt, G. Hüttman, and P. König, "Optical coherence microscopy for fast intravital imaging of airways in mice and humans with subcellular resolution," Pneumologie **69**(07), A50 (2015).
18. R. A. Leitgeb, M. Villiger, A. H. Bachmann, L. Steinmann, and T. Lasser, "Extended focus depth for Fourier domain optical coherence microscopy," Opt. Lett. **31**(16), 2450–2452 (2006).
19. L. Liu, J. A. Gardecki, S. K. Nadkarni, J. D. Toussaint, Y. Yagi, B. E. Bouma, and G. J. Tearney, "Imaging the subcellular structure of human coronary atherosclerosis using micro-optical coherence tomography," Nat. Med. **17**(8), 1010–1014 (2011).
20. J. Holmes, "Theory and applications of multi-beam OCT," in *1st Canterbury Workshop on Optical Coherence Tomography and Adaptive Optics*, Proceedings SPIE (SPIE, 2008), 713908.
21. B. A. Standish, K. K. Lee, A. Mariampillai, N. R. Munce, M. K. Leung, V. X. Yang, and I. A. Vitkin, "In vivo endoscopic multi-beam optical coherence tomography," Phys. Med. Biol. **55**(3), 615–622 (2010).
22. P. Mouroulis, "Depth of field extension with spherical optics," Opt. Express **16**(17), 12995–13004 (2008).
23. R. C. Bakaraju, K. Ehrmann, E. B. Papas, and A. Ho, "Depth-of-Focus and its Association with the Spherical Aberration Sign. A Ray-Tracing Analysis," J. Optom. **3**(1), 51–59 (2010).
24. A. T. Friberg and E. Wolf, "Angular spectrum representation of scattered electromagnetic fields," J. Opt. Soc. Am. **73**(1), 26–32 (1983).
25. M. K. Kim, *Digital holographic microscopy principles, techniques, and applications*, Springer series in optical sciences (Springer, New York, NY [u.a.], 2011), pp. XVI, 237 S.
26. H. Schulz-Hildebrandt and G. Hüttmann, "Modelling the Influence of spherical and chromatic aberration on resolution and depth of field in OCT and OCM," Biomed. Opt. Express **in preparation** (2018).
27. M. K. Kim, "Principles and techniques of digital holographic microscopy," SPIE Rev. **1**, 018005 (2010).
28. C. J. R. Sheppard, "Super resolution in Confocal Imaging," Optik - International Journal for Light and Electron Optics **80**, 53 (1988).
29. T. R. Corle and G. S. Kino, "Confocal scanning optical microscopy and related imaging systems," (Acad. Press, San Diego [u.a.], 1996).
30. R. A. M. Abdul, "Quantitative Measurement of Cellular Dynamics using Spectral Domain Optical Coherence Phase Microscopy," Dissertation (University of Lübeck, Lübeck, 2013).
31. H. Schulz-Hildebrandt, M. Münter, M. Ahrens, H. Spahr, D. Hillmann, P. König, and G. Hüttmann, "Coherence and diffraction limited resolution in microscopic OCT by a unified approach for the correction of dispersion and aberrations," in *Second Canterbury Conference on Optical Coherence Tomography (2CCOT),* A. G. Podoleanu and O. Bang, eds. (SPIE, University of Kent, Canterbury, UK, 2017).
32. D. Hillmann, T. Bonin, C. Lührs, G. Franke, M. Hagen-Eggert, P. Koch, and G. Hüttmann, "Common approach for compensation of axial motion artifacts in swept-source OCT and dispersion in Fourier-domain OCT," Opt. Express **20**(6), 6761–6776 (2012).
33. B. C. Flores, "Robust method for the motion compensation of ISAR imagery," Proc. SPIE **1607**, 512–517 (1992).
34. J. A. Nelder and R. Mead, "A Simplex Method for Function Minimization," Comput. J. **7**(4), 308–313 (1965).
35. P. Thévenaz, U. E. Ruttimann, and M. Unser, "A pyramid approach to subpixel registration based on intensity," IEEE Trans. Image Process. **7**(1), 27–41 (1998).
36. J. Schindelin, I. Arganda-Carreras, E. Frise, V. Kaynig, M. Longair, T. Pietzsch, S. Preibisch, C. Rueden, S. Saalfeld, B. Schmid, J. Y. Tinevez, D. J. White, V. Hartenstein, K. Eliceiri, P. Tomancak, and A. Cardona, "Fiji: an open-source platform for biological-image analysis," Nat. Methods **9**(7), 676–682 (2012).
37. F. J. Harris, "On the use of windows for harmonic analysis with the discrete Fourier transform," Proc. IEEE **66**(1), 51–83 (1978).

Biomedical Optics EXPRESS

38. D. Hillmann, G. Franke, C. Lührs, P. Koch, and G. Hüttmann, "Efficient Holoscopy image reconstruction," Opt. Express **20**(19), 21247–21263 (2012).
39. T. S. Ralston, D. L. Marks, P. S. Carney, and S. A. Boppart, "Interferometric synthetic aperture microscopy," Nat. Phys. **3**(2), 129–134 (2007).
40. M. Born, E. Wolf, and A. B. Bhatia, *Principles of optics electromagnetic theory of propagation, interference and diffraction of light,* 7., (expanded) ed. (Cambridge Univ. Press, Cambridge [u.a.], 2013), pp. XXXIII, 952 S.
41. J. W. Goodman, *Introduction to Fourier Optics,* 3rd ed. (Roberts & Co. Publishers, Englewood, Colo, 2005), pp. XVIII, 491 S.
42. J. M. Schmitt, S. H. Xiang, and K. M. Yung, "Speckle in Optical Coherence Tomography," J. Biomed. Opt. **4**(1), 95–105 (1999).
43. A. L. Oldenburg, R. K. Chhetri, D. B. Hill, and B. Button, "Monitoring airway mucus flow and ciliary activity with optical coherence tomography," Biomed. Opt. Express **3**(9), 1978–1992 (2012).
44. S. Bermbach, K. Weinhold, T. Roeder, F. Petersen, C. Kugler, T. Goldmann, J. Rupp, and P. König, "Mechanisms of cilia-driven transport in the airways in the absence of mucus," Am. J. Respir. Cell Mol. Biol. **51**(1), 56–67 (2014).
45. K. K. Chu, C. Unglert, T. N. Ford, D. Cui, R. W. Carruth, K. Singh, L. Liu, S. E. Birket, G. M. Solomon, S. M. Rowe, and G. J. Tearney, "In vivo imaging of airway cilia and mucus clearance with micro-optical coherence tomography," Biomed. Opt. Express **7**(7), 2494–2505 (2016).
46. Q. Fang, A. Curatolo, P. Wijesinghe, Y. L. Yeow, J. Hamzah, P. B. Noble, K. Karnowski, D. D. Sampson, R. Ganss, J. K. Kim, W. M. Lee, and B. F. Kennedy, "Ultrahigh-resolution optical coherence elastography through a micro-endoscope: towards in vivo imaging of cellular-scale mechanics," Biomed. Opt. Express **8**(11), 5127–5138 (2017).
47. D. Cui, K. K. Chu, B. Yin, T. N. Ford, C. Hyun, H. M. Leung, J. A. Gardecki, G. M. Solomon, S. E. Birket, L. Liu, S. M. Rowe, and G. J. Tearney, "Flexible, high-resolution micro-optical coherence tomography endobronchial probe toward in vivo imaging of cilia," Opt. Lett. **42**(4), 867–870 (2017).
48. K. Aanæs, "Bacterial sinusitis can be a focus for initial lung colonisation and chronic lung infection in patients with cystic fibrosis," J. Cyst. Fibros. **12**(Suppl 2), S1–S20 (2013).
49. U. Oltmanns, K. Palmowski, M. Wielpütz, N. Kahn, E. Baroke, R. Eberhardt, S. Wege, M. Wiebel, M. Kreuter, F. J. Herth, and M. A. Mall, "Optical coherence tomography detects structural abnormalities of the nasal mucosa in patients with cystic fibrosis," J. Cyst. Fibros. **15**(2), 216–222 (2016).
50. C. H. Feng, M. D. Miller, and R. A. Simon, "The united allergic airway: connections between allergic rhinitis, asthma, and chronic sinusitis," Am. J. Rhinol. Allergy **26**(3), 187–190 (2012).
51. E. A. Illing and B. A. Woodworth, "Management of the upper airway in cystic fibrosis," Curr. Opin. Pulm. Med. **20**(6), 623–631 (2014).

1. Introduction

Histology of excised tissue is the state-of-the-art diagnostic tool for a large number of major diseases like tumors, inflammatory or metabolic disorders. Beside invasiveness for obtaining the tissue sample, a major drawback of classical histology is, that it provides information only for one time point. Dynamic processes like mucus transport [1] which are potential important in lung diseases like cystic fibrosis cannot be observed. Intravital microscopy (IVM) offers the opportunity to image also the dynamics of disease related tissue changes. IVM does not only give insight into pathological mechanisms, it may also replace biopsies by virtue of a non-invasive optical biopsy. Clinical applications of IVM can be found for example in dermatology [2, 3], ENT [4] and ophthalmology [5, 6]. Here, the tissue of interest is readily accessible to high NA objectives. The examination of tissues inside the body needs the combination of high-resolution imaging with endoscopy. Laser scanning endo-microscopy was demonstrated for imaging small and large intestine [7–9] and other tissues [10]. Though it is able to provide dynamic imaging with cellular resolution, the main drawbacks are a fixed working distance and the limitation to 2-dimensional en-face imaging. Thus, only morphologic changes of a single cell layer are directly visualized and *in vivo* histological like cross-sectional imaging gets very challenging and time consuming due to the missing depth information.

Optical coherence tomography (OCT) uses interference of broad-band light to generate cross-sectional images similar to ultrasound [11, 12]. Using high NA imaging optics [13] and infrared radiation with several hundred nanometer spectral width [14], OCT with microscopic resolution (mOCT) can be used for a volumetric IVM [15–17]. However, one fundamental problem has to be overcome. By increasing lateral resolution of OCT, Rayleigh length and consequently the axial field of view (FOV), in which full lateral resolution is provided,

Biomedical Optics EXPRESS

decreases rapidly. Due to the high sensitivity of OCT, depth range is effectively not limited by the intensity fall-off in the out-of-focus planes caused by confocal gating, but by the reduced lateral resolution. The small axial FOV is a serious problem when examining awake humans or animals due to inevitable motion that results in displacement of the area of interest. Considerable efforts were made to overcame this problem by extending the axial FOV using Bessel beams [18], apodized Gaussian beams [19] or scanning with multiple foci [20, 21]. All these approaches have their disadvantages, either decreasing resolution or increasing imaging time.

For investigating cellular dynamics in the human mucosa, we developed and built a graded-index (GRIN) lens based optics for endo-microscopic OCT (emOCT) with increased depth of field, which provides cross-sectional images of mucosal tissue at 1.25 µm resolution and allows to image dynamic processes at rates of up to 80 frames per second (fps). The GRIN endoscope introduces chromatic and spherical aberrations which effectively increase the length of the beam waist [22, 23] but only slightly decreases the lateral resolution. To evaluate the detrimental effects of these aberrations on OCT imaging, we simulated the image performance numerically. Wave front aberrations of the endoscope were measured and calculated by ray tracing. With this data, Fourier optics and angular spectrum based beam propagation were used to simulated emOCT image formation under the influence of chromatic and spherical aberrations. *In vivo* imaging of human nasal mucosal structures with cellular resolution and measurement of mucus transport is demonstrated with our custom build GRIN endoscope.

2. Method

2.1 Simulation of OCT image formation

The influences of aberrations on OCT imaging were modeled based on single scattered photons. This approximation is usually valid for OCT imaging and allows to simulate image formation by deterministic concepts of Fourier optics and beam propagation based on the decomposition of the amplitude of the light field into spatial Fourier components [24, 25] instead of using Monte Carlo simulations. The algorithms are described in detail elsewhere [26]. In short, for each wavenumber which is detected by the FD-OCT spectrometer, the complex-valued illumination point spread function (PSF) was calculated for a truncated Gaussian beam in presence of an aberrations simulating phase function. Using the angular spectrum algorithm [24, 27], the complex-valued optical field distribution was propagated to the focus volume. This way, amplitude and phase of a three-dimensional PSF were calculated for each wavenumber. In the presence of chromatic aberration, the focal length was adjusted accordingly.

Scanned confocal imaging was simulated by a convolution of the object reflectivity with squared illumination PSF. This approach was used earlier to simulate confocal laser scanning microscopy [28, 29]. Depth resolution of OCT was simulated by integrating the confocal image in each pixel with the correct phase over the depth and adding a reference wave at each wavenumber. The simulated spectrally encoded detector signal was then calculated by squaring of the absolute value of the complex-valued interfering waves and multiplication with the spectral distribution of the broad-band light source used in the measurement setup.

The simulated data were processed by standard routines for the reconstruction of FD-OCT data including apodization, filtering and Fourier transformation [30]. All calculations were done with Matlab (Matlab 2015a, Mathworks, Natick, MA, USA).

2.2 High resolution GRIN endoscope

The custom-build GRIN endoscope (Grintech, Jena, Germany) consisted of a low NA GRIN rod, which acted as a relay optic, and a high NA GRIN lens serving as the microscope objective (Fig. 1). This doublet design provides a maximal imaging NA of 0.5 at a

Biomedical Optics EXPRESS

magnification of 2.6. Total length was 45 mm at a diameter of 1 mm. The GRIN optics was incorporated into a stainless-steel housing with an outer diameter of 2.75 mm and connected to a modified OCT scanner (OCTG, Thorlabs GmbH, Dachau, Germany), consisting of two galvanometer mirrors for the beam deflection and a collimator. The collimated light from the scanning optics was focused by an achromatic lens (49-948, Edmund Optics, Barrington, USA) into the back focal plane of the endoscope, which is situated approximately 100 µm in front of the end face of the GRIN rod. By reducing the entrance pupil diameter to 1.2 mm an NA of only 0.24, slightly less than half of the full NA of the GRIN optics, was employed for imaging. This lead to an Airy disk radius of 1.90 µm and full width half maximum of the theoretical point spread function of 1.15 µm. The lateral field of view was limited by the GRIN rod to approximately 200 µm.

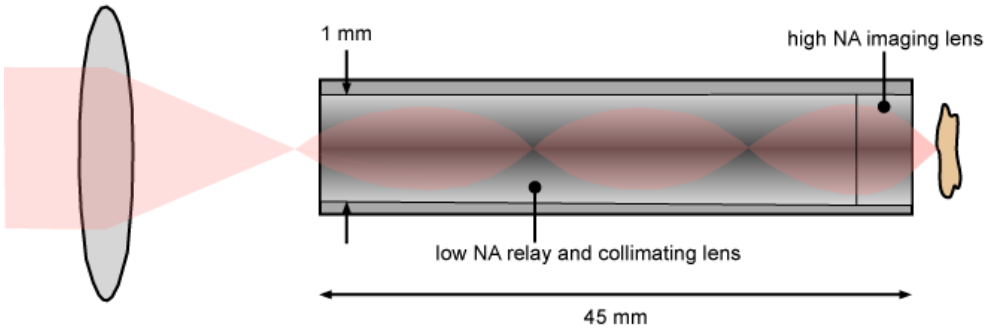

Fig. 1. Schematics of the optical design of the endoscope with the scanning lens, the low NA relay and collimating GRIN rod lens and the high NA imaging lens. Outer diameter was only 1 mm, the working distance 0.25 mm.

2.3 OCT setup

The emOCT (see Fig. 2) used a supercontinuum light source (320 Mhz repetition rate, NKT Photonics, Denmark), a wide band fiber beam splitter (Fiber Coupler 670, Thorlabs GmbH, Dachau, Germany) and a customized 400 nm bandwidth spectrometer (Thorlabs GmbH, Dachau, Germany). Light between 550 and 950 nm was coupled via a dichroic filter (SuperK Split, NKT Photonics, Denmark) and a single mode fiber (FD-7, NKT Photonics, Denmark) to the interferometer.

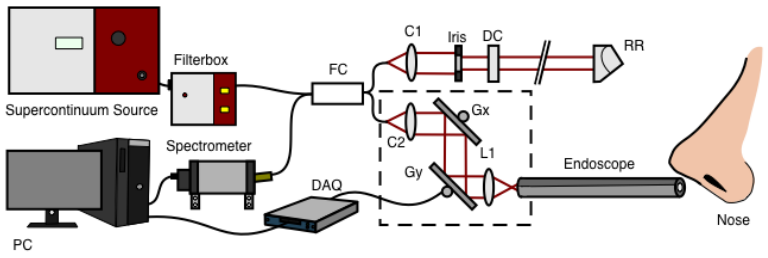

Fig. 2. Schematic illustration of the emOCT setup. FC: 50:50 fiber coupler; C1, C2: collimators; DC: dispersion compensation; RR: retroreflector; Gx, Gy: galvanometer mirror; L1: scanning lens; DAQ: digital analog converter. For detailed explanation see main text.

In the reference arm, the light was collimated (60FC-4-A18-02, Schäfter & Kirchhoff, Hamburg, Germany) and guided through a variable iris for adjusting the reference intensity and dispersion compensating customized SF57 substrate (Casix Inc., Fujian, China) onto a retro-reflector. The OCT scanner and the endoscope were connected to the second port of the fiber coupler. Reference and sample light were combined by this fiber coupler and guided to the spectrometer, which used a high-speed line scan CMOS camera (Basler Sprint, Basler, Ahrensburg, Germany) with up 127 kHz line rate at 2048 pixels to detect the interference in

Biomedical Optics EXPRESS

the wavelength range between 550 and 950 nm. Depending on the number of A-scans (512 or 1024), the effective imaging speed (including dead time) was either 160 or 80 fps. Timing and driving of the galvanometer mirrors were controlled by a data acquisition box (NI-USB-6251, National Instruments, Munich, Germany). Acquisition, processing, and visualization of OCT images were done using ThorImage software (Thorlabs GmbH, Dachau, Germany). To achieve a bandwidth limited axial resolution group velocity dispersion was compensated by adding the SF57 substrate to the reference arm and numerical compensation, which can also handle sample induced dispersion [31]. The measured interference spectra were converted with help of a Hilbert transform into a complex function. The dispersion related phase error was then compensated by subtracting the correcting phase function which was approximated by a up to the 9^{th} order polynomial [32]. The polynomial coefficients were calculated by optimizing image quality according to the Shannon metric [33] using the Nelder-Mead simplex algorithm [34].

2.4 Measurement of aberrations

For the simulation of the influence of aberrations on OCT imaging formation, monochromatic aberrations were measured using a Shack-Hartmann sensor (WFS150-5C, Thorlabs GmbH, Dachau, Germany). The GRIN endoscope was illuminated through the scanning lens by an 840 nm superluminescence diode (BLM-S-840-B-I-20, Superlum, Dublin, Ireland). By using a well characterized, essentially aberration-free microscope objective the light from the focus was collimated onto the Shack-Hartmann sensor.

Longitudinal chromatic aberrations were determined by placing, a gold mirror on a motorized table (Labjack MJL050, Thorlabs GmbH, Dachau, Germany) under the endoscope. The reference arm was blocked, and all 2048 pixel of the OCT spectrometer were recorded, while the gold mirror was shifted in 1 µm steps through the focus. Shifts of the depth, at which the maximum signal was detected, were attributed to the longitudinal chromatic aberrations.

2.5 Measurement of spatial resolutions

For comparison with the expected value, the lateral resolution at different depth was measured using 40 nm beads (Fluospheres, ThermoFisher Scientific Inc, Waltham, USA) embedded in Sylgard polymer (Dow Corning, Wiesbaden, Germany). Full width at half maximum (FWHM) was determined from a fit of a Gaussian function to the linear OCT signal in the en-face image of a single beads. At a fixed focus position, images of beats in different depths were evaluated to determine the axial dependence of the lateral resolution.

Axial resolution was determined as the FHWM of the linear OCT signal of the reflection at a dielectric surface.

2.6 Sample preparation and measurements

The use of resected conchae nasales from patients was approved by the ethics committee of the University of Lübeck, Germany (No. 04-158). For comparison with histology, semi-thin histological sections of the samples were stained with methylene blue-azure II.

In vivo measurements were conducted in a healthy subject at the concha nasalis media. The endoscope was inserted into the nose without local anesthesia. For index matching and to avoid irritant reactions, a drop Vidisic ED0 (Bausch + Lomb, USA) was placed on the tip of the endoscope. For comparison epithelium of nasal vestibule was imaged in a healthy subject with a commercially available OCT device (Telesto, Thorlabs GmbH, Dachau, Germany), which provided approximately 10 µm axial and 15 µm lateral resolution at 1300 nm central wavelength.

Post processing, which included motion compensation by rigid registration [35] of the frames of time series, and visualization were done with the open source software Fiji [36].

Biomedical Optics EXPRESS

3. Results

3.1 Optical performance of the endoscope

The actual lateral resolution was found to be 1.25 µm at the focus plane when measured using nanobeads. This was slightly below the expected diffraction limited resolution of 1.15 µm. Compared to an aberration-free Gaussian beam of the same focal spot size, the lateral resolution decreased less outside the focus plane (Fig. 3(a)). In our endoscope, it stayed below 2 µm over a depth range of 35 µm instead of only 15 µm for the Gaussian beam. The Rayleigh length of this Gaussian beam would be below 4.5 µm and the FWHM of the beam would degrade from 1.25 µm to less than 2 µm within 7 µm. In the endoscope, 2 µm lateral resolution was kept over more than 15 µm. At 20 µm defocus the lateral resolution would be degraded with a Gaussian beam to 4.5 µm instead of 2.5 µm.

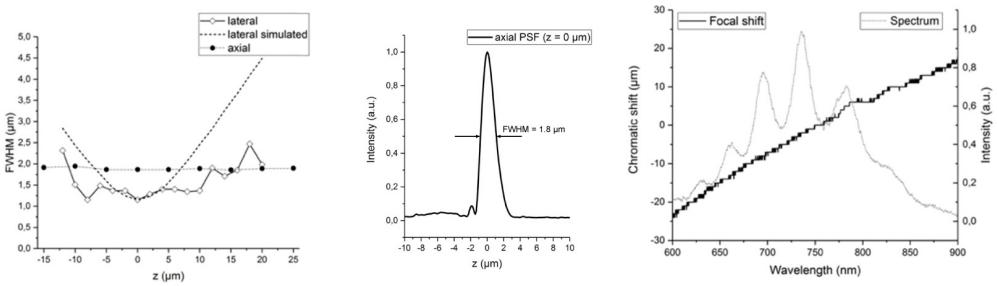

(a) (b) (c)

Fig. 3. (a) Axial (•) and lateral (o) resolution in different depth. For comparison of the expected resolution with an aberration-free Gaussian beam is shown (dashed line). The beam waist was scaled to the same size as the resolution measured in the focal plane. (b) Measured axial resolution at the focal point. (c) Chromatic focal shift at different wavelength (dark line), which contributes according to the power spectrum of the light source (grey line) to the OCT signal.

The 2.3-fold extended axial depth of focus, is caused by spherical and chromatical aberrations, which change the focal position for rays traveling at different angles to the optical axis and at different wavelengths, respectively. For the endoscope, we measured a focal shift of approximately 0.14 µm per nm wavelength which leads to more than 40 µm shift over the complete spectrum (Fig. 3(c)) which was used for emOCT imaging. This exceeds confocal gating by 2.5 times and degrades axial resolution by reducing the effective spectral width which can be used for OCT imaging. We measured 1.8 µm FWHM of the axial PSF in water (Fig. 3(a), 3(b)) instead to the expected 1.35 µm. Width and shape of the axial PSF depend on spectral width and apodization during the processing of the A-scans [37]. The theoretical value of 1.35 µm for a Hann window apodized spectrum reaching from 550 nm to 950 nm was verified with a dispersion-balanced Michelson interferometer. In the endoscope, chromatic aberrations decreased the effective spectral width of light, which was detected from a certain depth, and lead to a reduced axial resolution. In summary, the endoscope aberrations increase imaging depth by 2.3-fold at cost of less than 30% - 40% decrease in axial resolution.

Lateral wave front aberrations of 3.8 lambda were measured with the wavefront sensor for the endoscope and the additional optics. This was twice the value calculated from data provided by the manufacturer for the endoscope. The difference is probably caused by aberrations of the collimator which optical layout was not known to us, and imperfections resulting from the GRIN manufacturing process.

Biomedical Optics EXPRESS

3.2 Impact of aberration on the image formation

The impact of the spherical and chromatic aberrations on the OCT image is quite complex since OCT is a coherent imaging modality, where interference between the images of different object structures and speckle dominate the resulting image. For a better understanding, we simulated OCT imaging in the presence of the aberrations, which were measured for the endoscope. We compared aberration-free emOCT imaging with imaging with spherical aberration (3.8 wavelengths), chromatic focal shift (0.14 µm/nm) and with combined aberrations (Fig. 4). As expected, at the focal plane the simulated image of the test object are best resolved without aberrations. However, with increasing distance from the focus the test structures were better visible with aberrations. Without aberrations, the defocus at 30 µm blurs all small structures. In contrast, all simulated structures are visible with spherical aberrations.

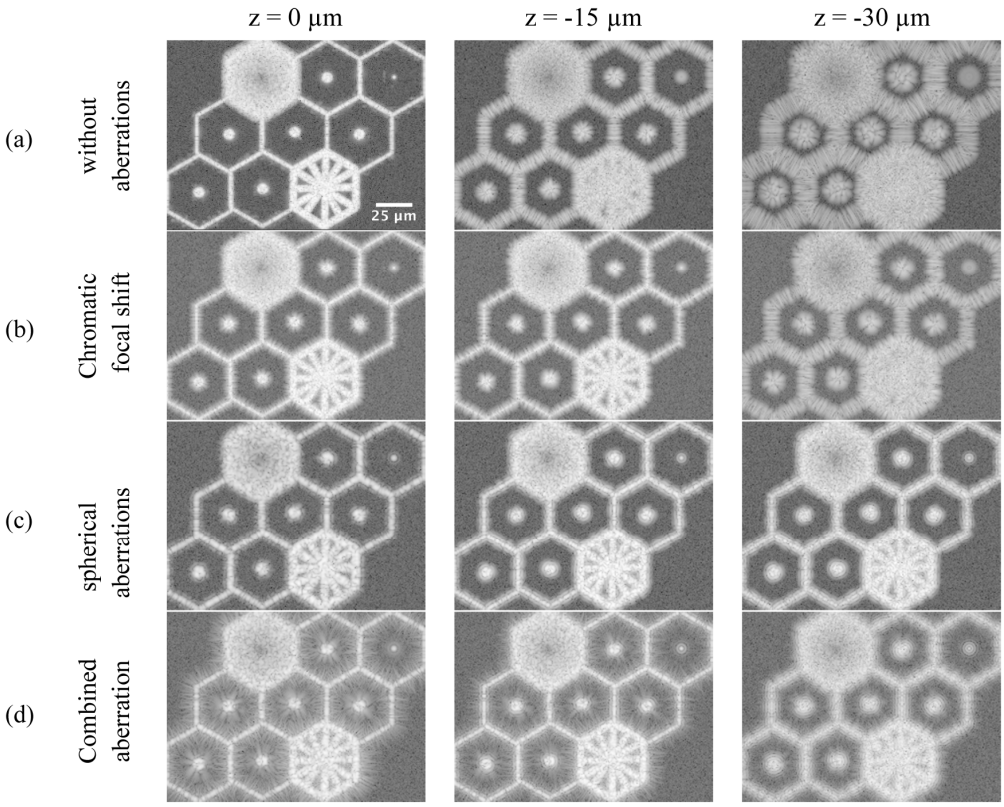

Fig. 4. (a) Simulation of emOCT imaging without aberrations (a), chromatic aberrations (b), spherical aberrations (c), and the combination of both aberrations (d). Simulated aberrations correspond to the aberrations measured for the endoscope.

Already, 15 µm outside the focus the cartwheel structure is only visible in the presence of aberrations. Spherical aberrations seem to work better than chromatic aberrations.

3.3. In vivo measurements of human nasal mucosa

The high lateral resolution and the increased depth-of-field of the endoscope improved *in vivo* imaging in humans considerably. Several microscopic structures in the epithelium and the connective tissue, which were not visible with common OCT devices at 10 µm resolution, are clearly seen (Fig. 5). The different layers of stratified squamous epithelium of the nasal vestibule and blood vessels (v) were visible. After reducing the speckle noise by averaging

Biomedical Optics EXPRESS

four images, resolution is even good enough to visualize single epithelial cells (arrow in Fig. 5). Increased visualization of cellular structures in B-scans in a field of view of 200 µm is due to a 5 to 10 times increased axial and lateral resolution. Just increasing the lateral resolution would not allow to image cellular structures in B-scans but can visualize cellular structures in en-face images as we previously demonstrated [16].

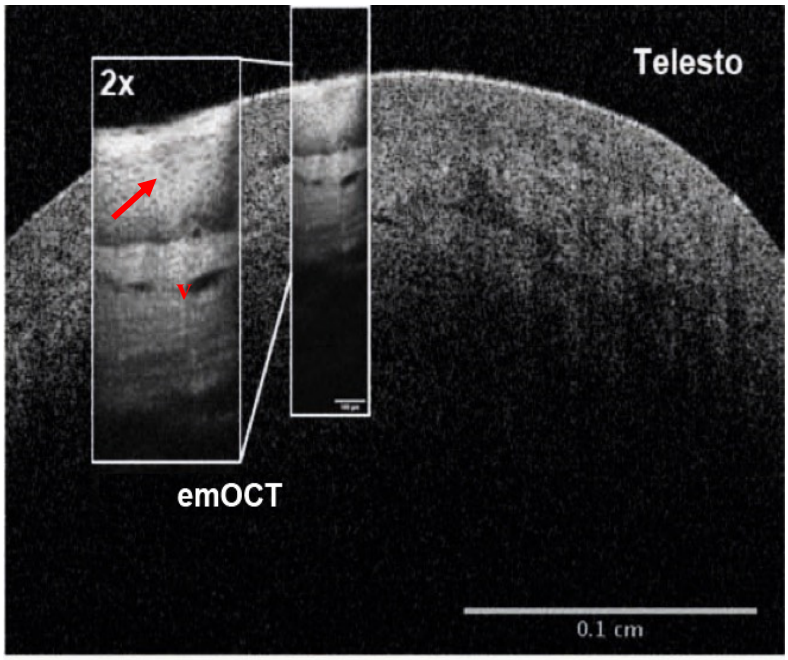

Fig. 5. Comparison of a 1300 nm OCT image with 10 µm lateral resolution to the emOCT imaging (inset) taken from the same tissue at different positions. Both images of nasal stratified squamous epithelium in the vestibule of the nose were taken *in vivo* and scaled to the same size. emOCT visualizes otherwise barely visible vessels (v) with high quality and even single cells can be seen (arrow).

Comparison of methylene blue-azure II stained histological sections of the nasal concha to images of the concha obtained *in vivo* showed that emOCT is able to identify glands, vessels, fibrous structures and even cilia at the pseudostratified respiratory epithelium (Fig. 6). Due to difficulties of positioning the endoscope *in vivo*, we were not always able to resolve single epithelial cells. However, the border between the epithelial cells and the lamina propria was seen in all cases, as well as glands and vessels. The imaging frame rate of 80 Hz allowed to observe the motion of single erythrocytes. In addition, mucus above the surface was visible. Despite the increased focus length, image quality in the different depth layers still depended on the position of the focus, as the total depth of imaged tissue was a few hundred micrometers.

Biomedical Optics EXPRESS

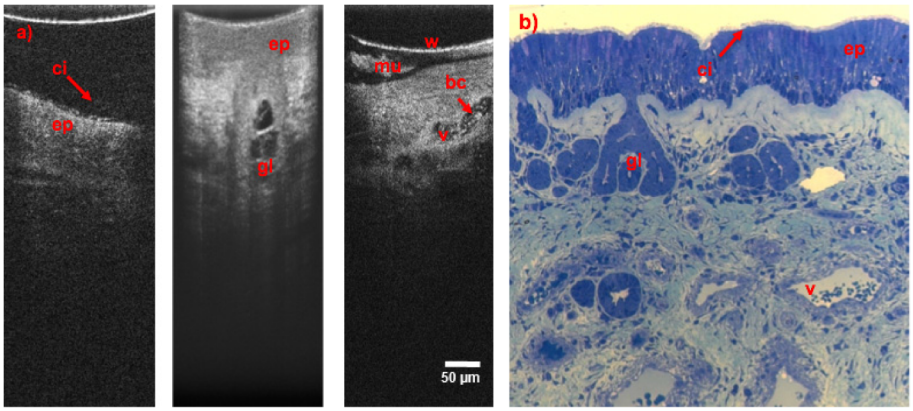

Fig. 6. Comparison of endoscopic OCT images recorded *in vivo* (a) with a representative methylene blue-azure II stained histological section of a nasal concha (b). Resolution of the emOCT is sufficient to resolve cilia (ci) and individual blood cells (bc) in vessels (v). Mucosal epithelium (ep) and glands (gl) are delineated from the underlying connective tissue by a different texture, which resembles cellular and fibrous structures. Mucus (mu) is often visible between the epithelium and the bright line generated by the end window (w) of the endoscope. In contrast to histology, emOCT is able to visualize dynamics processes like cilia motion, blood flow and mucus transport in the tissue (see Visualization 1).

The high imaging frame rates, allowed also to quantify mucus transport in the presence of bulk motion. Figure 7 and Visualization 2 show the transport of the mucus layer (mu) on top of the epithelium (ep). After correction of bulk motion by rigid registration, lateral motion in the mucus layer was determined by tracking single flakes inside the mucus (asterix). Imaging speed was high enough to follow each flake until it left the either the field of view or the plane of the B-scan. Both was easily visible and the position of the flake over time could be recorded usually over a few tens of micrometers (Fig. 7(d)). From these data the average speed of the mucus was calculated, which was in this case 165 µm/s over half a second. This value is higher than expected from cilia-driven transport. However, because the imaging was taken during nasal breathing we assumed the inspiration [1] increased to the transport velocity. As a control, the movement of the epithelium was also evaluated (Fig. 7(c)). As expected, the tissues did effectively not move consistently over time.

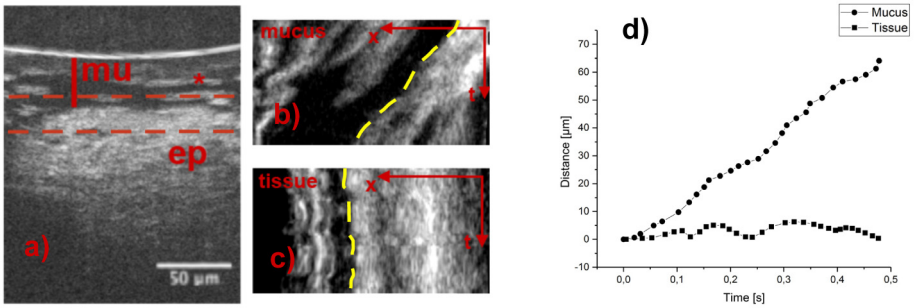

Fig. 7. Measurement of mucus transport inside the human nose. Times series of B-scans show the motion of the layer mucus on top of the epithelium *in vivo* (a and Visualization 2). By following motion of structures in a plane of the mucus layer (upper red dashed line, b) a transport velocity (yellow dashed line) can be determined. Plotting the OCT signal in the dashed lines over time (b, c) allows to determine changes of the lateral position of characteristic structures of mucus and epithelium. The slope of these positions over time (d) is the lateral motion velocity. In the epithelium (lower red dashed line) no net tissue motion was seen (c, d).

Biomedical Optics EXPRESS

4. Discussion

One of the main advantages of OCT imaging is decoupling axial resolution from the imaging NA. Only the spectral bandwidth of the irradiation determines depth resolutions. This is no longer valid in the presence of aberration. Chromatic aberrations shift the focus of the different spectral components. Different spectral bands therefore contain information from different depth. This increases the depth of focus, but also degrades the axial resolution by damping the spectral components. Although not obvious, spherical aberrations also influence the axial resolution. Destructive interference between aberrated beams blank out certain wavelength components on the optical axis [26]. This also can lead to a reduced axial resolution and side lobes in the axial PSF outside the focal depth. In contrast to dispersion mismatch between the interferometer arms, degradation of the axial resolution by aberrations cannot be compensated unless full phase coherence is established in the imaged volume as in holoscopy or ISAM [38, 39].

Fortunately, the influence of aberrations on the axial resolution is usually modest. Though our endoscope had considerable chromatic and spherical aberrations an axial resolution better than 2 µm was maintained over the whole imaging depth.

At the NA of 0.24, in the focal plane a nearly isotropic resolution below 2 µm was achieved, which was barely degraded by the aberrations. But both, spherical and chromatic aberrations, caused an elongation of the focus. In the case of chromatic aberrations, the focal point for each wavelength is different which spreads the focus, whereas in spherical aberrations the focus is spread due to radially dependence of the refractive power of the optics. The resulting focal shift scales with the square of the NA and is therefore much stronger than the degradation of the lateral resolution, which scales linearly with the NA [29]. The different dependences of lateral and axial dimensions of the focus on aberrations are the basis of the increased depth of view, which was used here successfully for emOCT imaging.

Increased depth of focus was already shown for spherical aberrations during conventional incoherent imaging [22, 23]. However, the beneficial effect on OCT imaging is not that obvious, since aberrations differently effect coherent and incoherent imaging [40, 41]. OCT imaging is dominated by speckle noise [42], which masks especially small round structures like cells or cell organelles. These speckle result from random interference from light within a resolvable voxel. In the presence of aberrations, point spread functions are broadened. In incoherent imaging, the overlap of broadened PSFs decreases the contrast of the structures. In OCT, the PSFs interfere and add to the high contrast speckle pattern. Already small contribution in the wings of the PSFs considerably contribute to the intensity distribution in the mOCT image.

For better understanding of this effect we conducted extensive simulations [26], which included speckle noise, defocus, and aberrations. Using imaging parameters of the emOCT, these simulations demonstrate the possibility of a significant increase of the axial FOV, increasing the depth range in which small cell-like structures can be distinguished. This behavior was very useful for the high-resolution OCT endoscope when imaging nasal mucosal tissue. Instead of an expected depth of field of only 9 µm for the NA of 0.24, OCT signal and lateral resolutions were maintained over 35 µm. Thereby, an excellent visibility of near cellular and, under optimal conditions, cellular structures was achieved *in vivo*.

The combination of high resolution, high imaging speed and cross-sectional imaging offers new opportunities for clinical diagnosis. Malfunction of mucociliary clearance is one of the key indicators for several diseases, like primary ciliary dyskinesia (PCD) or cystic fibrosis (CF). In these diseases, the dynamics of mucus transport and the driving motion of cilia in the epithelium play a significant role. Measurements of the mucociliary clearance *ex vivo* and in animals, with resolution in the range of 2.5 to 6 µm were successfully performed by several groups including our own [16, 17, 43–45]. Recently, high resolution endoscopic OCT with extended depth of field were presented by different groups using Bessel beams [18, 46] or apodized Gaussian beams [19, 47] with axial resolutions better then 2.5 µm. Bessel beams are

Biomedical Optics EXPRESS

very efficient in increasing the depth of field. High resolution OCT elastography was demonstrated in small animal [46]. However, no portable endoscopic systems were demonstrated so far and the Bessel beam introduces side lobes to the PSF, which contain significant amounts of energy. Sensitivity and image quality are decreased compared to a Gaussian beam. µOCT uses a Gaussian beam a split aperture with an outer ring for illumination and the central aperture for detection. Using this design, in which image quality suffers also considerably from side lobes in the PSF, an endoscope was designed for imaging pulmonary diseases in humans [47]. It provides a lateral resolution of 4 µm, a depth of field 170 µm and up to 40 frames per second. This resolution was not sufficient for imaging of cellular structure.

The ability to measure ciliary action and mucus transport in humans is of great interest for the diagnosis of these diseases. However, high NA endoscopes for emOCT imaging, which are needed to access human lower airways, are not available. The easiest access to airway tissue is at the nasal mucosa. The concha nasalis can be examined from the front side by an only 5 cm long rigid endoscope. Here already cilia and mucus can be found and various studies have shown, that in CF morphological changes and functional impairments occurs. With low resolution endoscopic OCT, it was shown that CF leads to a change and structural abnormalities in the nasal mucosa [48–51]. Here we have shown that high resolutions around 1.5 µm provides additional information which cannot be seen with clinical systems or similar extend depth of field endoscopes at lower lateral resolution. Imaging of the nasal airways is far less invasive than bronchoscopy of the lower airways and is therefore easier to perform in the clinical setting. The here presented rigid endoscope offers sufficient resolution for volumetric imaging of cilia function and mucus transport. In contrast to confocal laser endoscopy, B-scans are visualized which show the different tissue layers without exact positioning in the distance to the tissue surface. Interactively, the relevant layers can be brought into the focus volume. EmOCT offers new options for simple minimal invasive diagnoses or monitoring of therapeutic effects on parameters such as mucus transport or morphological changes.

5. Summary

We present a high-resolution OCT micro-endoscope for imaging nasal tissue in humans. Spherical and chromatic aberrations of the GRIN based endoscopic optics increase the depth of field at only moderate loss in lateral and axial resolution. Characteristic structures of human nasal tissue were seen *in vivo* in cross-sectional images (B-scans), which are usually only seen in histological sections. The high imaging speed of up to 160 fps, allowed averaging up to four B-scans for speckle noise reduction, while still imaging at video rate.

In future, the new endoscope can be used for diagnosis and treatment control of different lung diseases like cystic fibrosis or primary ciliary dyskinesia.

Funding

German Minister of Research, Helmholtz Center Munich of Health and Environment DZL-ARCN (82DZL001A2).

Disclosures

The authors declare that there are no conflicts of interest related to this article.